

Comparison between 6-band and 14-band $\mathbf{k}\cdot\mathbf{p}$ formalisms in SiGe/Si heterostructures

M. El kurdi, G. Fishman, S. Sauvage, and P. Boucaud*

Institut d' Electronique Fondamentale, UMR CNRS 8622, Bâtiment 220, Université Paris-Sud, 91405 Orsay, France

(Received 10 February 2003; published 23 October 2003)

We report on a comparison between a 14-band and a 6-band $\mathbf{k}\cdot\mathbf{p}$ model to describe the valence band of pseudomorphic SiGe/Si heterostructures. A strong variation between both models is observed for the description of the valence band dispersion and for the calculation of the intersubband dipolar matrix elements for in-plane wave vectors as small as 10% of the Brillouin zone size. We show that the 6-band formalism overestimates the amplitude of the intersubband absorption by a factor of 2 for light polarized in the layer plane. The origin of the polarization of the intersubband transitions is discussed and the limits of both models for the calculation of the energy band diagram and dipole matrix elements are outlined. We finally show that the usual axial approximation procedure, which is often used to build a cylindrical 4-band or 8-band Hamiltonian, cannot give a cylindrical 14-band Hamiltonian.

DOI: 10.1103/PhysRevB.68.165333

PACS number(s): 73.21.Fg, 78.20.Bh, 78.67.De

I. INTRODUCTION

Infrared transitions in SiGe/Si low-dimensional heterostructures have attracted considerable interest in recent years. The intersubband transitions in quantum wells and the intraband transitions in quantum dots have an important potential for optoelectronic devices operating in the midinfrared or far-infrared spectral ranges.^{1,2} Midinfrared photodetectors using quantum wells or quantum dots epitaxially grown on silicon have been demonstrated.^{3,4} More recently, intersubband electroluminescence in cascade structures has been reported, opening the route to the realization of a silicon-based midinfrared or far-infrared laser.⁵ A large band discontinuity between silicon and strained SiGe alloys is observed in the valence band, implying that the intersubband or intraband optical processes involve different hole states (heavy holes, light holes, and spin-orbit split-off band). Many of the infrared optical experiments on strained SiGe quantum wells or quantum dots reported so far are thus interpreted in the framework of a 6-band $\mathbf{k}\cdot\mathbf{p}$ calculation.³ This formalism corresponds to a resolution of the Luttinger Hamiltonian that describes the Γ_8^+ and Γ_7^+ valence bands.⁶ The main advantage of this approach is to avoid the computation of the conduction band while taking into account its influence on the valence band energy diagram and on the optical intervalence band transitions. The influence of the conduction band on the valence band energies is introduced by second-order perturbation with the Luttinger parameters.⁷ The influence of the conduction band on the intervalence band optical matrix elements is obtained by first-order $\mathbf{k}\cdot\mathbf{p}$ perturbation on the valence band states.⁸ The introduction of the first-order $\mathbf{k}\cdot\mathbf{p}$ perturbation to account for the conduction band states can be used to calculate the optical matrix elements of intersubband transitions in quantum wells.⁹ One important consequence of the effect of the conduction band on intersubband optical transitions in quantum wells is the possibility to observe optical transitions for light polarized parallel to the layer plane, as evidenced in several absorption experiments.¹⁰ Since the interband separation between valence and conduction states near the Γ point is large in Si and Ge materials, it is justified to take into account the conduction band by a perturbation of first order on the valence band states.

In the case of SiGe alloys, the s -type and p -type conduction bands are not far in energy and both bands exhibit interaction matrix elements with the valence band of the same order of magnitude. It is therefore necessary to introduce a 14-band $\mathbf{k}\cdot\mathbf{p}$ formalism for SiGe/Si quantum wells to account for the admixture between the first s -type and the p -type conduction bands on the valence band.¹¹ The 14-band formalism describes the whole conduction band and the valence bands [Γ_8^- , Γ_6^- , Γ_7^- , Γ_8^+ , Γ_7^+]. In this formalism, the influence of the first s -type and p -type conduction bands on the valence band is included exactly. It appears that the interaction between the p -type conduction band and the p -type valence band favors intersubband transitions parallel to the layer plane while the interactions of both s - and p -type conduction bands with the valence band have nearly equal contributions to the oscillator strength parallel to the growth axis. Since the 14-band formalism accounts for the interaction between the conduction band and valence band exactly, it should be more accurate than the 6-band model. Significant differences exist between both models. We show that the axial approximation which is usually used in the 6-band theory is not valid with the 14-band model. The axial approximation is valid when we consider the influence of an s -type conduction band because it induces an isotropic effect on the valence band. It is not the case in the 14-band model since the p -type conduction band has an anisotropy effect on the valence band and we see no analytical method to build a 14×14 Hamiltonian with a cylindrical symmetry.

In this work, we report on a detailed comparison between the 6-band and 14-band formalism for the calculation of the energy band diagram and the dipolar matrix elements of SiGe/Si heterostructures. We show that important differences are obtained for the subband energies in quantum wells at wave vectors smaller than 1 nm^{-1} along with strong variations in the dipolar matrix elements when the in-plane wave vector increases, leading to significant differences in the calculation of the absorption spectrum in p -doped structures. We find that the 6-band model gives higher absorption amplitudes for the $\text{HH}_1\rightarrow\text{HH}_2$ transition (by 20%) and for the $\text{HH}_1\rightarrow\text{LH}_1$ transition (factor of 2) as compared to the absorption amplitude obtained with the 14-band model in heavily doped structures.

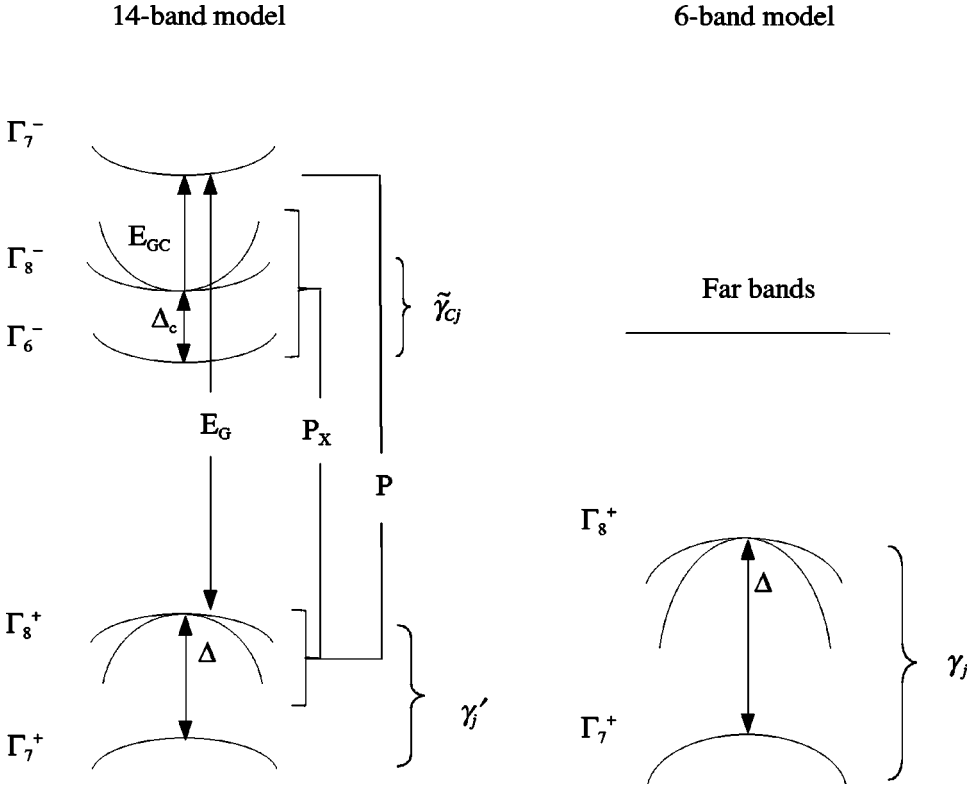


FIG. 1. Schematic representation for the 14- (left) and 6- (right) band models representing the involved bands and relevant parameters.

This article is organized as follows. In Sec. II, the 14- and 6-band models are first described and their results are compared for the case of bulk silicon. We point out the limit of validity of the 14-band model to describe the valence band, because of the uncertainty of the input parameters which are involved in describing the nonparabolicity of the p -type conduction band. While the 14-band model does not allow us to describe accurately the dispersion of the conduction bands near the Γ point, we discuss its influence on the calculation of the valence band energy diagram for wave vectors close to the center of the Brillouin zone. We finally quantify the limit of both models and show that the 14-band model is still more accurate than the 6-band model. In Sec. III, we provide a detailed description of the valence band of a strained Si/Si_{0.5}Ge_{0.5}/Si quantum well. We present a comparison between both formalisms, focusing on the energy band diagram and on the dipolar matrix elements. Both intersubband ($HH_1 \rightarrow HH_n$) and intervalence band [$HH_1 \rightarrow LH_n(SO_n)$] transitions are studied. We point out the strong variations of the energies and of the dipolar matrix elements between the 6-band and 14-band models for wave vectors smaller than 10% of the Brillouin zone size, in particular for the case of the $HH_1 - LH_1(SO_1)$ transition. In Sec. IV, a discussion of the axial approximation is finally presented.

II. 14-BAND AND 6-BAND $\mathbf{k} \cdot \mathbf{p}$ FORMALISMS

In this section, we first describe both 14-band and 6-band formalisms and we present a comparison between both formalisms for the case of bulk silicon. We show the limitation of both models to describe the valence band. The main issue of this part is to show the strong nonparabolicity effect of the

p -type conduction band on the valence band energies. Second, we attempt to quantify the limit of both 6-band and 14-band models.

14-band and 6-band $\mathbf{k} \cdot \mathbf{p}$ formalism

The $\mathbf{k} \cdot \mathbf{p}$ equation we solve in the present work is^{6,8}

$$H_k U_{lk}^{(0)} = E_{lk}^{(0)} U_{lk}^{(0)}, \quad (1)$$

where

$$H_k = \frac{\mathbf{p}^2}{2m_0} + U + \frac{\hbar}{4m_0^2 c^2} (\nabla U \wedge \mathbf{p}) \cdot \boldsymbol{\sigma} + \frac{\hbar}{m_0} \mathbf{k} \cdot \mathbf{p} + \frac{\hbar^2 k^2}{2m_0}, \quad (2)$$

m_0 is the free electron mass, \hbar is the reduced Planck constant, and c is the speed of light in vacuum. U is the periodic potential of the unstrained crystal and $\boldsymbol{\sigma} = (\sigma_x, \sigma_y, \sigma_z)$ are the Pauli matrices. The $U_{lk}^{(0)}$ represent the Bloch function spinors in the unstrained crystal. As usual the k -dependent⁸ spin-orbit coupling term $(\hbar^2/4m_0^2 c^2) (\nabla U \times \mathbf{k}) \cdot \boldsymbol{\sigma}$, has been neglected. In the following, we apply the $\mathbf{k} \cdot \mathbf{p}$ formalism to the 14-fold space of the valence band [Γ_8^+, Γ_7^+], the lowest Γ_7^- , and the second conduction bands [Γ_8^-, Γ_6^-]. These bands and the associated parameters are schematically illustrated in Fig. 1. In the case of the 6-band model, the $\mathbf{k} \cdot \mathbf{p}$ equation (2) is projected onto the 6-fold space of valence bands [Γ_8^+, Γ_7^+]. The Γ bands are defined in an orthogonal base of Bloch states at $k=0$ given in Table I. This set of functions diagonalizes the spin-orbit coupling represented by the third term in Eq. (2). The notations J and J_z in Table I represent the total angular momentum and its projection

TABLE I. Luttinger-Kohn periodic amplitudes used in both 14- and 6- (right) band models. The indices $-$ and $+$ design, respectively, the conduction (left) and valence (right) states while $|+\rangle$ and $|-\rangle$ are the s -type spin-degenerated conduction states. The set of wave functions for the 6-band model is the same without the conduction states. The phases are chosen to give real matrix elements to the $\mathbf{k} \cdot \mathbf{p}$ Hamiltonian.

Γ_8^- $J=\frac{3}{2}$ $J_z=\pm\frac{3}{2};\pm\frac{1}{2}$	Γ_8^+ $J=\frac{3}{2}$ $J_z=\pm\frac{3}{2};\pm\frac{1}{2}$
$ -\frac{3}{2}\rangle = \left i \left[-\frac{1}{\sqrt{2}}(X_C + iY_C)\uparrow \right] \right\rangle$	$ +\frac{3}{2}\rangle = \left i \left[-\frac{1}{\sqrt{2}}(X + iY)\uparrow \right] \right\rangle$
$ -\frac{1}{2}\rangle = \left i \left[-\frac{1}{\sqrt{6}}(X_C + iY_C)\downarrow + \sqrt{\frac{1}{2}}Z_C\uparrow \right] \right\rangle$	$ +\frac{1}{2}\rangle = \left i \left[-\frac{1}{\sqrt{6}}(X + iY)\downarrow + \sqrt{\frac{2}{3}}Z\uparrow \right] \right\rangle$
$ -\frac{1}{2}\rangle = \left i \left[\frac{1}{\sqrt{6}}(X_C - iY_C)\uparrow + \sqrt{\frac{2}{3}}Z_C\downarrow \right] \right\rangle$	$ +,\frac{1}{2}\rangle = \left i \left[\frac{1}{\sqrt{6}}(X - iY)\uparrow + \sqrt{\frac{2}{3}}Z\downarrow \right] \right\rangle$
$ -\frac{3}{2}\rangle = \left i \left[\frac{1}{\sqrt{2}}(X_C - iY_C)\downarrow \right] \right\rangle$	$ +,\frac{3}{2}\rangle = \left i \left[\frac{1}{\sqrt{2}}(X - iY)\downarrow \right] \right\rangle$
Γ_6^- $J=\frac{1}{2}$ $J_z=\pm\frac{1}{2}$	Γ_7^+ $J=\frac{1}{2}$ $J_z=\pm\frac{1}{2}$
$ -\rangle = \left i \left[\frac{1}{\sqrt{3}}(X_C + iY_C)\downarrow + \sqrt{\frac{1}{3}}Z_C\uparrow \right] \right\rangle$	$ +\rangle = \left i \left[\frac{1}{\sqrt{3}}(X + iY)\downarrow + \sqrt{\frac{1}{3}}Z\uparrow \right] \right\rangle$
$ -\rangle = \left i \left[\frac{1}{\sqrt{3}}(X_C - iY_C)\uparrow - \sqrt{\frac{1}{3}}Z_C\downarrow \right] \right\rangle$	$ +\rangle = \left i \left[\frac{1}{\sqrt{3}}(X - iY)\uparrow - \sqrt{\frac{1}{3}}Z\downarrow \right] \right\rangle$
Γ_7^- $J=\frac{1}{2}$ $J_z=\pm\frac{1}{2}$	
$ +\rangle = S\uparrow\rangle$	
$ -\rangle = S\downarrow\rangle$	

along the z growth axis, respectively. The first index $+$ ($-$) denotes the valence (conduction) states which are even (odd) under the inversion symmetry operator, respectively. In Table I, the functions $X, Y, Z, S, X_C, Y_C,$ and Z_C are defined as the eigenstates of the H_U Hamiltonian: $H_U = \mathbf{p}^2/2m_0 + U$. These functions are assumed to be real and have, respectively, Γ_5^+ symmetry (X, Y, Z), Γ_2^- symmetry (S) and Γ_4^- symmetry (X_C, Y_C, Z_C) of the cubic symmetry group \mathcal{O}_h .

The 6×6 and 14×14 $\mathbf{k} \cdot \mathbf{p}$ matrices are given in Appendix A by Eq. (A1) and in Appendix B by Eq. (B1), respectively. In the case of the 14-band formalism, two key points are to be clarified. The first point is related to the values of the modified Luttinger parameters γ'_j ($j=1,2,3$) which appear in the off-diagonal terms inside the $[\Gamma_8^+, \Gamma_7^+]$ subspace. The values of γ'_j are chosen to highlight the effect of the whole remote bands on the valence bands, except for the first s -type and p -type conduction bands which are included exactly. The values of γ'_j are deduced from the well-known Luttinger parameters γ_j as presented in Appendix B [see Eq. (B2)]. We note that the expression of the parameter γ'_j is equivalent to the one used in the 8-band model,¹² which is, for instance, extensively used to describe the $[\Gamma_6^-, \Gamma_8^-, \Gamma_7^-]$ valence and conduction bands in GaAs heterostructures. The second key point is related to the values of the off-diagonal terms inside the $[\Gamma_8^-, \Gamma_6^-]$ conduction bands. These terms include the remote band effects on the p -type conduction

band, without the valence and the Γ_7^- bands, through the $\tilde{\gamma}_{Cj}$ Luttinger-like parameters. In Eq. (B3) of Appendix B, we give the relation between the $\tilde{\gamma}_{Cj}$ parameters and γ_{Cj} parameters which include the whole remote band effect on the $[\Gamma_8^-, \Gamma_6^-]$ conduction bands. In this work we consider the s -type conduction band without any remote band influence. If the remote band effects are not taken into account in the off-diagonal terms inside the $[\Gamma_8^-, \Gamma_6^-]$ subspace, the p -type conduction band is parabolic like. As will be explained below, a parabolic dispersion of the p -type conduction band in bulk Si and Ge would be quite different from the well-known dispersion¹³ especially in the $[100]$ direction of k space. At first order, one can assume that a nonparabolic contribution to the conduction band will not influence the valence band if it is weak as compared to the interband energy separation. This assumption can be illustrated with a simple two-band model. The $\mathbf{k} \cdot \mathbf{p}$ Hamiltonian without the spin-orbit coupling,

$$H'_k = H_U + \frac{\hbar}{m_0} \mathbf{k} \cdot \mathbf{p} + \frac{\hbar^2 k^2}{2m_0}$$

can be written inside the (U_C, U_V) basis as

$$H'_k = \begin{bmatrix} E_G + \varepsilon(k) + \frac{\hbar^2 k^2}{2m_0} & Pk \\ Pk & \frac{\hbar^2 k^2}{2m_0} \end{bmatrix}, \quad (3)$$

where U_C and U_V represent the conduction and valence band states, respectively, E_G is the interband separation energy defined as $H'_k|U_C\rangle = (E_G + \hbar^2 k^2/2m_0)|U_C\rangle$ with $H'_k|U_V\rangle = (\hbar^2 k^2/2m_0)|U_V\rangle$, and $P = (\hbar/m_0)\langle U_C|p_z|U_V\rangle$. Here $\varepsilon(k)$ is an energy which is referred to as the nonparabolicity of the conduction band induced by the remote band effect. For small wave vectors, we have $Pk \ll E_G$ and at third order of perturbation the valence band energy can be written as

$$E_V = \left[1 - \frac{E_P}{E_G} \left(1 - \frac{\varepsilon}{E_G} \right) \right] \frac{\hbar^2 k^2}{2m_0}, \quad (4)$$

where E_P is related to the matrix element P by $E_P = (2m_0/\hbar^2)P^2$. Equation (4) is equivalent to the Kane equation, which gives the effective mass of holes, corrected by a term depending on $\varepsilon(k)$. For a given wave vector k , if E_G is large as compared to the nonparabolicity contribution $\varepsilon(k)$, we can neglect the effect of the nonparabolicity of the conduction band on the valence band. While the nonparabolicity of the p -type conduction band is strong near the Γ point in Si and Ge materials, the use of the 14-band Hamiltonian without the $\tilde{\gamma}_{Cj}$ which includes the remote band influence is thus limited to a given range of k where $E_G \gg \varepsilon(k)$. According to Eq. (4), a variation of 10% is observed for the energy of the valence band between the case $\varepsilon = E_G/10$, which is reasonable following Ref. 13, and the case $\varepsilon = 0$ at $k = 1 \text{ nm}^{-1}$.

We now turn to the influence on the valence band of the 14×14 matrix including the effect of the remote bands on the p -type conduction band as compared to the same matrix without taking into account the influence of the remote bands. Figure 2 shows the conduction band (a) and valence band (b) energy diagrams of bulk silicon obtained with the 14-band model. The figures present a comparison between $H_k^{14 \times 14}$ without accounting for $\tilde{\gamma}_{Cj}$ (solid line) and with $\tilde{\gamma}_{Cj}$ (dotted line). Since the conduction band parameters involved in this 14×14 Hamiltonian are not well known, we chose to test their influence by taking values of $\tilde{\gamma}_{Cj}$ which leads to a flat p -type conduction band by putting $\gamma_{Cj} = 0$ [see Appendix B, Eq. (B3)]. We observe that the k dependence of the p -type conduction band influences very rapidly the valence band dispersion curve when the wave vector increases. An energy variation of 8% is found at 1 nm^{-1} for the heavy-hole band when we take into account the influence of the remote bands on the p -type conduction band. We note that there are no experimental cyclotron resonance data available for the conduction band parameters γ_{Cj} near the Γ point as opposed to the case of the valence band since electrons in bulk Si and Ge do not fill the Γ conduction band states. It is in contrast with direct band gap materials where the parameters of the conduction band can be experimentally measured. The accuracy of the 14-band model to calculate the dispersion curves of the valence bands thus depends on the type of investigated semiconductors. In order to avoid the uncertainty with the 14-band model for Si and Ge due to the conduction band nonparabolicity, a more extended formalism which includes remote band states like the sp^3s^* method would be necessary.¹⁴ Such an extended model can be used as a refer-

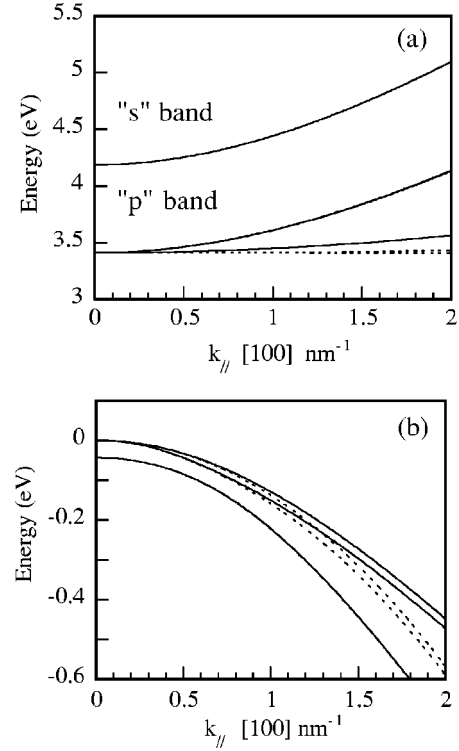


FIG. 2. (a) Conduction band and (b) valence band of bulk silicon calculated with the 14×14 matrix including the $\tilde{\gamma}_{Cj}$ as dashed lines and without the $\tilde{\gamma}_{Cj}$ parameters as solid lines. The $\tilde{\gamma}_{Cj}$ account for the remote band influence on the p -type conduction band. The valence band is influenced by the p -type conduction band very rapidly as the wave vector increases.

ence to determine the limit of validity of the 6-band and 14-band models for the valence band calculation near the Γ point.

The second-order perturbation used in the 6-band model to include remote band effects on valence states through the Luttinger parameters is justified when the $\mathbf{k} \cdot \mathbf{p}$ coupling with other bands is weak as compared to the interband separation. In the two-level Hamiltonian of Eq. (3), this situation corresponds to $Pk \ll E_G$ or $k \ll E_G \times \sqrt{2m_0/\hbar^2 E_P}$ where E_G is the difference of energy at the Γ point and E_P the momentum matrix elements between U_C and U_V . If we consider an upper value $k_{\text{lim}} = \frac{1}{10} (E_G \times \sqrt{2m_0/\hbar^2 E_P})$ for the range of k where the 6-band model is valid, a numerical application with $E_G = 3.4 \text{ eV}$ and $E_P = 25 \text{ eV}$ gives a wave vector limit of 0.34 nm^{-1} .

Figure 3 shows the valence band dispersion of bulk silicon performed with the 6-band (solid line) and 14-band (dashed line) models in the $[100]$ direction. It clearly shows that the 6-band model does not describe the dispersion like the 14-band model and that variations between both models increase quadratically with the wave vector. While the 14-band model is limited by the description of the p -type conduction band nonparabolicity, the 6-band model is limited by the validity of second-order perturbation. As both models present different types of limitation to describe the valence band, we attempt to quantify their limit and to define which of the 6-band and 14-band formalisms is more accurate by

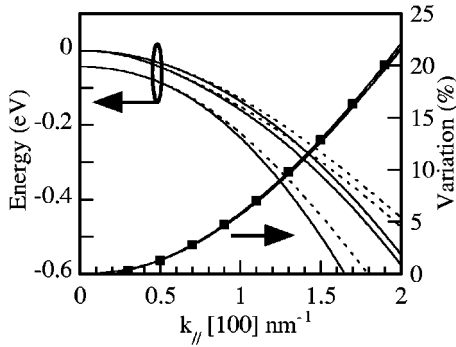


FIG. 3. Valence band of bulk silicon calculated with the 14-band model as dashed lines and the 6-band model as solid lines. Relative variations between the different subbands are depicted in the right scale.

using a comparison with the description of the valence band as presented in Ref. 14. In Fig. 4(a) we show the valence band energy diagram obtained with the sp^3s^* model as a solid line as compared with the energy diagram obtained with the 14-band Hamiltonian (dashed line) without including the remote band influence on the p -type conduction band and the 6-band model (dotted line). We obtain a good agreement between the 14-band and the sp^3s^* model while the difference with the 6-band model appears clearly. The limitation of the 14-band model to describe the valence band due

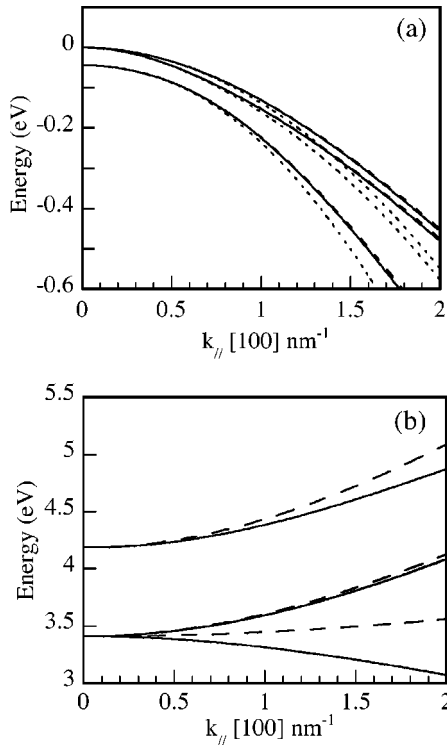


FIG. 4. (a) Valence band diagram obtained with the sp^3s^* model as solid lines compared with the 14-band Hamiltonian (dashed line) without including remote band effect on the p -type conduction band and the 6-band model (dotted line). (b) conduction band obtained with the sp^3s^* (solid line) and the 14-band model without including the remote band effect on the p -type conduction band (dashed line).

to the uncertainty in the input parameters is thus not so strong. This is in agreement with the assumption that the remote bands are so far in energy that their effect can be neglected in the range of wave vector we have considered (2 nm^{-1}).¹¹ We can thus conclude that the 6-band model is more limited than the 14-band model despite the lack of knowledge of the conduction band parameters. In the following, the 14×14 matrix will be used without including remote band effects on the p -type conduction band. The comparison of the sp^3s^* with the 14-band formalism for the case of the conduction band is presented in Fig. 4(b). The agreement is less satisfying as compared to the valence band but the difference is not significant for the description of the valence intersubband dipole matrix elements as checked by modifying arbitrarily the values of $\tilde{\gamma}_{Cj}$.

III. 6-BAND AND 14-BAND $k \cdot p$ METHOD FOR STRAINED SiGe/Si QUANTUM WELLS

We will illustrate below the differences between the 6-band and 14-band models for the case of a strained $\text{Si}_{0.5}\text{Ge}_{0.5}/\text{Si}$ quantum well. This case is of interest since it can be used as a first approximation to describe the optical properties of the self-assembled islands obtained by nominally depositing pure Ge on Si.¹⁵

A. Valence band dispersion

To describe the valence band dispersion of a strained SiGe/Si quantum well grown along the z axis on a (001) silicon substrate, we solve the equation

$$H\psi = [H_k + H_S + V(z)]\psi = E\psi, \quad (5)$$

where $V(z)$ is the band offset potential which is diagonal in both 14-14- and 6-6-dimensional spinor basis. The strain potential is included with the Hamiltonian H_S following the procedure described in Ref. 16. For a quantum well grown on a [001]-oriented substrate and thin enough to elastically accommodate the strain due to the lattice mismatch, the strain in the (001) plane is

$$\varepsilon_{xx} = \varepsilon_{yy} = \varepsilon_{\parallel} = \frac{a_{\text{Si}} - a_{\text{Si}_{1-x}\text{Ge}_x}}{a_{\text{Si}_{1-x}\text{Ge}_x}}, \quad (6)$$

where a_{Si} and $a_{\text{Si}_{1-x}\text{Ge}_x}$ are the lattice constants of the substrate material (Si) and the well material ($\text{Si}_{1-x}\text{Ge}_x$), respec-

TABLE II. This table gives the experimental parameters involved into the strain potential for Si and Ge. The lattice parameters are given in \AA . The deformation potentials taken in the H_S Hamiltonian (a_C for the conduction band and a_V , b_V for the valence bands) are given in eV. $a_G = a_C - a_V$ is the gap deformation potential. C_{11} and C_{12} are the elastic moduli given in MPa. All parameters are taken from Ref. 27 except for b_V (Ref. 17). We use a linear interpolation to obtain the strain parameters for a SiGe alloy.

	a (\AA)	a_C	a_V	a_G	b_V	C_{11}	C_{12}
Si	5.431	-5.10	0	-5.10	2.33	1.675	0.65
Ge	5.658	-9.5	0	-9.5	2.08	1.315	0.494

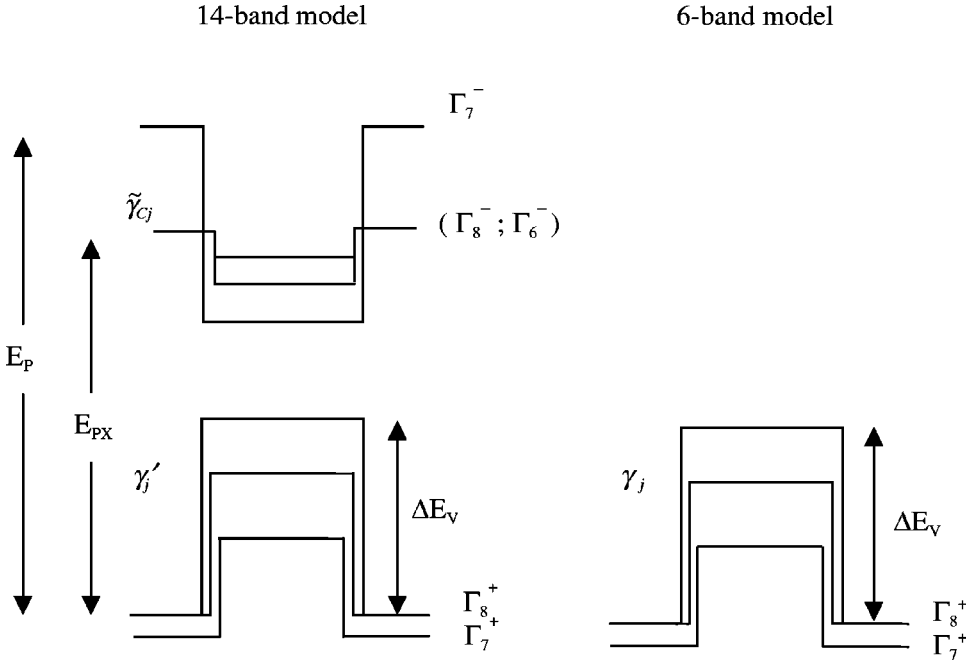


FIG. 5. Band offsets for valence and conduction bands including the diagonal elements of the strain potential in the set of the spinor basis given in Table I. Left: 14-band model. Right: 6-band model.

tively. The condition of zero stress in the z direction gives $\varepsilon_{zz} = \varepsilon_{\perp} = -2(C_{12}/C_{11})\varepsilon_{\parallel}$ while $\varepsilon_{xy} = \varepsilon_{yz} = \varepsilon_{zx} = 0$. Here C_{11} and C_{12} are the elastic stiffness constants. The strain Hamiltonian H_S induces a shift and a splitting of the confining potential seen by the carriers. The strain Hamiltonian matrix elements can be obtained from the $\mathbf{k} \cdot \mathbf{p}$ matrix elements by symmetry considerations and substitution of the corresponding terms $k_{\alpha}k_{\beta} \rightarrow \varepsilon_{\alpha\beta}$ with $\alpha, \beta = x, y, z$.¹⁶ The H_S matrices used for the calculation of the energy band diagram with the 14-band model and 6-band model are given by Eq. (B4) of Appendix B and Eq. (A2) of Appendix A, respectively. The parameters involved into the Hamiltonian H_S are given in Table II. Figure 5 shows the band diagram at the Γ point of a strained Si/Si_{0.5}Ge_{0.5}/Si quantum well. In this figure the strain effect on the band edge energies was taken into account. The origin of energy is taken at the top of the heavy-hole band barrier. The numerical values for the Si and Si_{0.5}Ge_{0.5} band parameters used in this work are given in Table III. In the following, the results are illustrated for the case of a 5-nm-thick Si/Si_{0.5}Ge_{0.5}/Si quantum well. The heavy-hole valence band offset for the strained material ΔE_V is assumed to be 350 meV.¹⁷ Using the usual assumption in the envelope-function approach that the basis $|\pm, J_z\rangle$ is the same in both materials Si and SiGe, we replace k_z by the momentum operator $\hat{k}_z = -i\partial/\partial z$ in the H_k Hamiltonian. The solution of Eq. (5) at a given k_{\parallel} is written in the form

$\psi_{k_{\parallel}}(z) = \sum_n^{6 \text{ or } 14} \chi_{n,k_{\parallel}}(z)|n\rangle$ where $\chi_{n,k_{\parallel}}(z)$ is the envelope function. The index n refers to the states $|\pm, J_z\rangle$ given in Table I. In order to account for the spatial dependence along the z axis of the band parameters $a(z)$ and for the boundary conditions, the second-order terms in \hat{k}_z in the 6×6 and 14×14 $\mathbf{k} \cdot \mathbf{p}$ matrices, like $a(z)\hat{k}_z^2$, are replaced with $\hat{k}_z a(z)\hat{k}_z$,^{18,19} while the linear terms like $a(z)\hat{k}_z$ are replaced with $(1/2)[\hat{k}_z a(z) + a(z)\hat{k}_z]$.¹⁹ Equation (5) is solved using a Fourier-like series expansion of the envelope function $\chi_{n,k_{\parallel}}(z)$, a method appropriate to account for the boundary conditions.¹⁹ To describe a quantum well centered at $L/2$, an efficient and suitable basis of function

$$|\varphi_m\rangle = \sqrt{\frac{2}{L}} \sin\left(\frac{m\pi}{L}z\right)$$

has been used to project the envelope function as $\chi_{n,k_{\parallel}}(z) = \sum_{m=1}^N c_m^{n,k_{\parallel}} |\varphi_m\rangle$. By using this set of basis, the envelope function is imposed to be null at $z=0$ and $z=L$. The envelope function is by this way sampled with the first N eigenfunctions of a large well of width L with an infinite barrier potential. The width of the large well L and the number N of functions $|\varphi_m\rangle$ are taken such that the bound states are not influenced by the infinite barrier (of the large well) and by checking simultaneously the numerical convergence of the

TABLE III. Experimental band parameters of bulk Si and SiGe alloys used in this work. The Luttinger parameters γ_j are taken from Ref. 3 (see also Ref. 17). The energies gap E_G and E_{GC} , spin-orbit splitting Δ , and Δ_C in eV are taken following Ref. 27. The fixed values of the Kane energy E_P and E_{PX} in eV are considered as identical in the well and in the barrier.

	γ_1	γ_2	γ_3	E_{PX}	E_P	E_G	E_{GC}	Δ	Δ_C
Si	4.285	0.339	1.446	15	25	4.185	-0.775	0.044	0
Si _{0.5} Ge _{0.5}	5.9	0.9	2.0	15	25	2.54	0.725	0.165	0.093

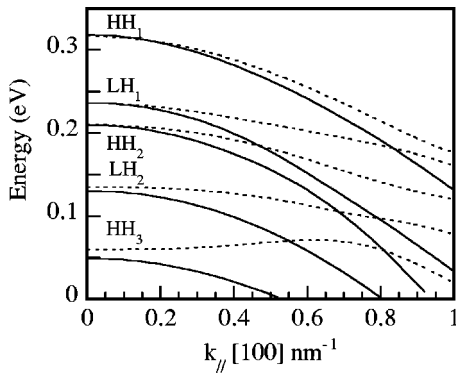


FIG. 6. Dispersion of the hole subbands in the [100] direction of the k space. The dispersions as dashed and solid lines are obtained with the 14-band and 6-band formalisms, respectively. From top to bottom, the subbands correspond to the HH_1 , $\text{LH}_1(\text{SO}_1)$, HH_2 , $\text{LH}_2(\text{SO}_2)$, and HH_3 subbands.

energies.²⁰ By applying the Hamiltonian H containing the potential $V(z)$ and the operator \hat{k}_z to the 14- (6-) dimensional basis $|\pm, J_z\rangle$ and developing each term into the N -dimensional basis $|\varphi_m\rangle$, the resolution of Eq. (5) is converted into a 14 (6) $N \times 14$ (6) N matrix eigensystem problem inside the 14 (6) N -fold $|\pm, J_z\rangle \otimes |\varphi_m\rangle$ new basis. After diagonalizing the 14 (6) $N \times 14$ (6) N matrices at several point of the (k_x, k_y) in-plane space, we obtain a correspondence of the band diagram of the hole-confined states with the corresponding wave functions. Since—as will be shown below—the axial approximation as proposed in Ref. 21 is not possible with the 14-band formalism, the numerical in-

vestigation was performed for in-plane wave vectors along the [100] direction. The following ideas remain valid for the other directions of the wave vector in the layer plane.

The valence band energy diagram of the 5-nm-thick strained SiGe/Si quantum well obtained after solving Eq. (5) is shown in Fig. 6 for the [100] direction. The 14- and 6-band model solutions are shown in dashed and solid lines, respectively. The energy of the first confined states are in good agreement between both models, but as the energy gets closer to the barrier edge (0 meV), a discrepancy between both models is observed. This behavior is associated with the increase of the wave vector when the quantized kinetic energy along k_z increases. As the confined states are related to large- k_z wave vectors, the variation of the valence subband energies obtained in quantum wells can be attributed to the differences in valence band dispersion found for bulk systems for values of k of $1-2 \text{ nm}^{-1}$. Figure 7 shows the projection of the wave function components $\chi_{n,0}(z)$ corresponding to each level obtained at $k_{\parallel}=0$ with the 6-band model. According to the wave function representation, the confined states are indexed from the top to the bottom as HH_1 , $\text{LH}_1(\text{SO}_1)$, HH_2 , $\text{LH}_2(\text{SO}_2)$, and HH_3 . Because the light-hole and spin-orbit split-off states are strongly mixed, we denote the state “LH(SO)” the “light-hole-like” state or, for short, “LH.”

The admixture of valence and conduction bands can occur at $k_{\parallel}=0$. Figure 8 shows each component $\chi_{n,0}(z)$ of the wave function as obtained with the 14-band model. It appears clearly that the heavy-hole states are exclusively mixed with the p -type conduction states and not with the s -type

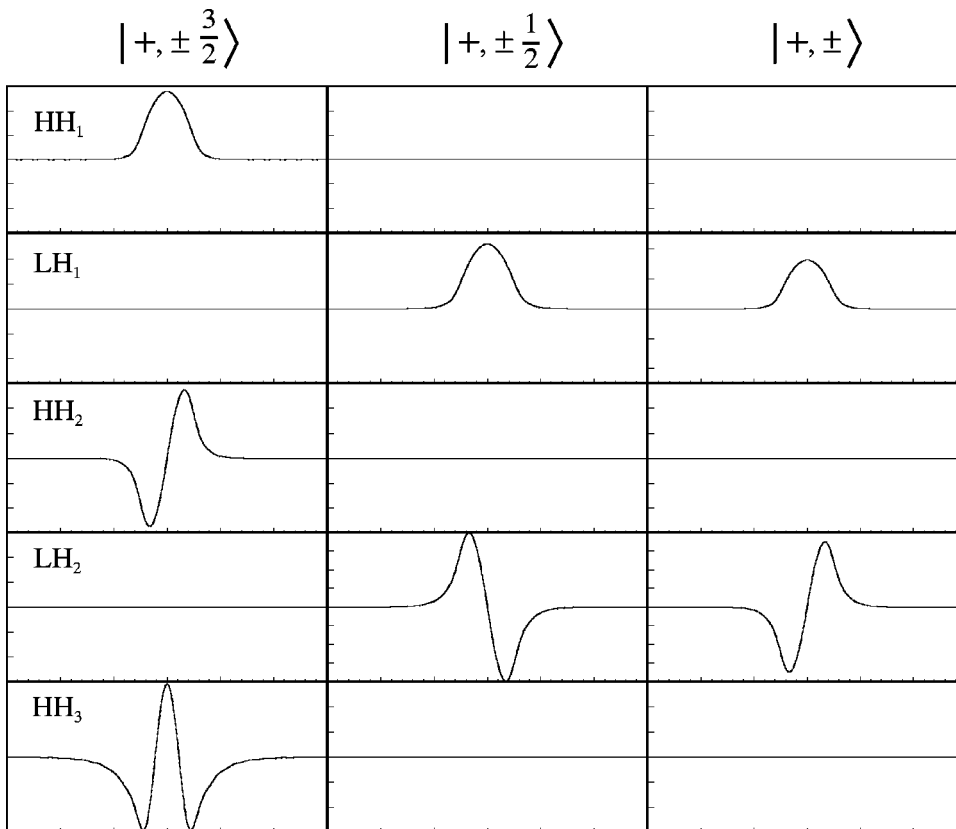


FIG. 7. Envelope function $\chi_{n,0}(z)$ representation of the hole confined states in a 5-nm-thick $\text{Si}_{0.5}\text{Ge}_{0.5}/\text{Si}$ quantum well calculated with the 6-band formalism. The corresponding levels are from top to bottom HH_1 , $\text{LH}_1(\text{SO}_1)$, HH_2 , $\text{LH}_2(\text{SO}_2)$, and HH_3 . We note that at $k_{\parallel}=0$ the heavy-hole subbands are not mixed, while the SO and LH subbands are strongly mixed. This mixing is due to both coupling inside the $\mathbf{k} \cdot \mathbf{p}$ Hamiltonian and the H_S Hamiltonian.

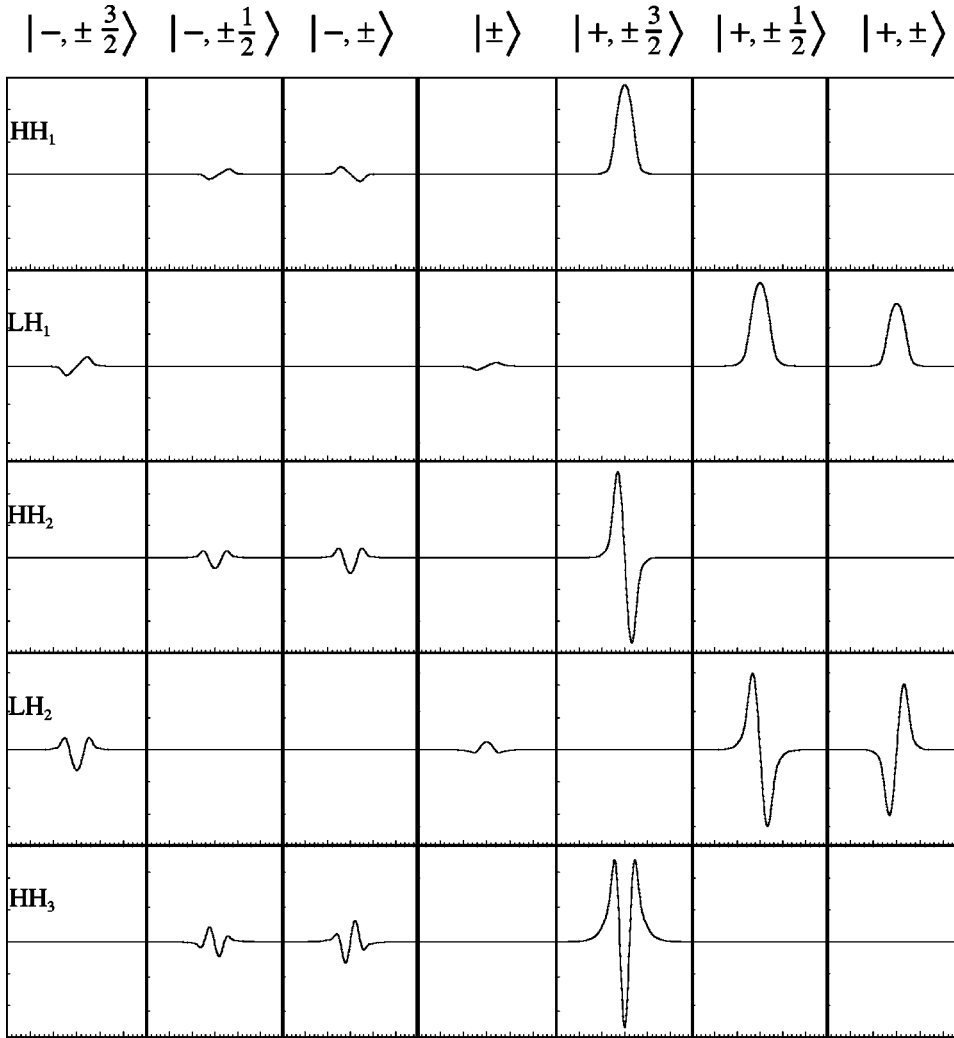


FIG. 8. Envelope function $\chi_{n,0}(z)$ representation of the hole confined states in a 5-nm-thick $\text{Si}_{0.5}\text{Ge}_{0.5}/\text{Si}$ quantum well calculated by the 14-band formalism. The corresponding levels, which are given by the band diagram in Fig. 5, are from top to bottom HH_1 , $\text{LH}_1(\text{SO}_1)$, HH_2 , $\text{LH}_2(\text{SO}_2)$, and HH_3 . We note that at $k_{\parallel}=0$ the heavy-hole subbands are not mixed with the s -like conduction band but only with the p -like conduction band. We expect the p -type conduction band to influence exclusively the $\text{HH}_1 \rightarrow \text{HH}_n$ optical transitions.

conduction states for a zero in-plane wave vector. This feature can be easily predicted by looking at the interband matrix elements inside the 14×14 matrix for $k_x = k_y = 0$. In this case there are no coupling terms between the $|+, \pm \frac{3}{2}\rangle$ and $|\pm\rangle$ states while the coupling of the $|+, \pm \frac{3}{2}\rangle$ states with the $|-, \pm\rangle$ and $|-, \pm \frac{1}{2}\rangle$ still exists. This feature is in contrast with the behavior of light-hole subbands $|+, \pm \frac{1}{2}\rangle$ which are mixed with both s -like $|\pm\rangle$ and p -like $|-, \pm \frac{3}{2}\rangle$ conduction bands. The light-hole subband mixing with both s - and p -type conduction bands at $k_x = k_y = 0$ can be easily explained by the fact that in this case the $|+, \pm \frac{3}{2}\rangle$ state is composed with (X, Y, Z) wave functions (Table I). The Z components of the light hole allow the $(\mathbf{k} \cdot \mathbf{p})_z$ coupling with the $|\pm\rangle$ state at $k_x = k_y = 0$.

B. Intersubband dipolar matrix elements

We now turn to the dipolar matrix element calculation for intersubband transitions from the HH_1 subband to the HH_2 , LH_1 , and LH_2 subbands. The interactions of s -type conduction and p -type conduction bands with the valence band have nearly equal contribution to the $\text{HH}_1 \rightarrow \text{HH}_2$ dipolar matrix element along the growth axis when $k_{\parallel} \neq 0$.¹¹ We show here that the dipole matrix element of this transition is mainly

influenced by the p -type conduction band and not by the s -type conduction band when $k_{\parallel} = 0$. The s -type conduction band influence occurs only when k_{\parallel} increases because of band-mixing effects. Another interesting property is that the $\text{HH}_1 \rightarrow \text{LH}_2$ transition is allowed at $k_{\parallel} = 0$ for light polarized in the (x, y) plane. This feature which is usually explained by the band-mixing effect is more detailed in the present work with an assignment of the specific bands at the origin of this effect, in particular to describe the influence of the conduction bands into the optical transitions $\text{HH}_1 \rightarrow \text{HH}_n$ and $\text{HH}_1 \rightarrow \text{LH}_n$ at $k_{\parallel} = 0$. The comparison of the data obtained with the 14-band model with the data obtained with the 6-band model indicates that strong differences are observed at small in-plane wave vectors, thus leading to significant differences in the absorption spectrum.

The calculation of the dipolar matrix element is obtained as follows. The momentum matrix element between an initial i state and a final f state is given by the expression^{9,22}

$$(\boldsymbol{\varepsilon} \cdot \mathbf{p})_{i,f} = \left(\frac{m_0}{\hbar} \right) \left\langle \boldsymbol{\varepsilon} \cdot \frac{\partial H_k}{\partial \mathbf{k}} \right\rangle_{i,f}, \quad (7)$$

where $\boldsymbol{\varepsilon}$ is a unit vector parallel to the light polarization. As the dipole operator is related to the momentum operator, we

chose in this work to discuss the dipolar matrix element given at k_{\parallel} by

$$(\boldsymbol{\varepsilon} \cdot \boldsymbol{\mu})_{i,f}^{k_{\parallel}} = \frac{e \left\langle \boldsymbol{\varepsilon} \cdot \frac{\partial H_k}{\partial \mathbf{k}} \right\rangle_{i,f}^{k_{\parallel}}}{\hbar \omega_{i,f}^{k_{\parallel}}}. \quad (8)$$

The term $\hbar \omega_{i,f}$ is the energy difference between the initial and final states. The computation of the dipole $(\boldsymbol{\varepsilon} \cdot \boldsymbol{\mu})_{i,f}$ is made by using the scalar product $\boldsymbol{\varepsilon} \cdot \nabla_{\mathbf{k}} H_k$. Starting from the bulk $\mathbf{k} \cdot \mathbf{p}$ Hamiltonian we perform two scalar products for the case $\boldsymbol{\varepsilon} = (\varepsilon_x, \varepsilon_y, 0)$ and the case $\boldsymbol{\varepsilon} = (0, 0, \varepsilon_z)$ in order to investigate separately the x, y and the z components of the optical transitions. We then obtain two matrices in which we replace k_z by \hat{k}_z . These matrices are given in Appendix C in the case $k_{\parallel} = 0$ and for the 6-band model. For the simplicity of the description of the matrix element we do not develop the terms like $a(z)\hat{k}_z$ into $\frac{1}{2}[\hat{k}_z a(z) + a(z)\hat{k}_z]$, but this development which is necessary for conservation of the current density at the interface between the well and barrier is made in the calculation of the matrix elements before projecting them onto the $|\varphi_m\rangle$ basis. After development of the matrix element into the N -fold basis $|\varphi_m\rangle$, we obtain two matrices $(\boldsymbol{\varepsilon} \cdot \partial H_k / \partial \mathbf{k})_{n_i, m_i, n_f, m_f}^{k_{\parallel}}$ of size $14(6)N \times 14(6)N$ which are used into the computation of the dipole along (x, y) and z by the expression

$$\left\langle \boldsymbol{\varepsilon} \cdot \frac{\partial H_k}{\partial \mathbf{k}} \right\rangle_{i,f}^{k_{\parallel}} = \sum_{m_f, n_f} \sum_{n_i, m_i} c_{m_f}^{n_f, k_{\parallel}^*} \left\langle \boldsymbol{\varepsilon} \cdot \frac{\partial H_k}{\partial \mathbf{k}} \right\rangle_{n_f + m_f, n_i + m_i}^{k_{\parallel}} c_{m_i}^{n_i, k_{\parallel}}. \quad (9)$$

The coefficients $c_m^{n, k_{\parallel}}$ and energies $\hbar \omega_{i,f}^{k_{\parallel}}$ involved in the computation of the dipoles are obtained from the diagonalization of the Hamiltonian H for a given k_{\parallel} . We use the index n and m to represent the function $|(\pm), J_z\rangle$ and the function $|\varphi_m\rangle$, respectively.

We note that the properties of the optical transitions can be observed in the $\boldsymbol{\varepsilon} \cdot \nabla_{\mathbf{k}} H_k$ matrix before its development into the N -fold basis $|\varphi_m\rangle$. Appendix C gives the matrix $\boldsymbol{\varepsilon} \cdot \nabla_{\mathbf{k}} H_k$ obtained from the 6-band $\mathbf{k} \cdot \mathbf{p}$ Hamiltonian presented in Appendix A [Eq. (A1)]. While the discussion is more simple with the analytical expression available in the 6-band model, we attempt to understand the effect of the s - and p -type conduction bands on the transitions from the HH_1 subband to the HH_n and LH_n subbands at $k_{\parallel} = 0$. This discussion can be supported by the previous observation made about Fig. 8 which shows the mixing of the valence band with the conduction band for the confined hole states of the well. In particular, the HH_n subbands are exclusively coupled with the p -type conduction band at $k_{\parallel} = 0$. In the following, in order to underline the contribution of the first s - and p -type conduction bands into the matrix $\boldsymbol{\varepsilon} \cdot \nabla_{\mathbf{k}} H_k$, we use the expression of the Luttinger parameter γ_j ($j = 1, 2, 3$) obtained inside the $[\Gamma_8^-, \Gamma_6^-, \Gamma_7^-, \Gamma_8^+, \Gamma_7^+]$ (see Ref. 25). When looking at the $\boldsymbol{\varepsilon} \cdot \nabla_{\mathbf{k}} H_k$ matrix for the case $\boldsymbol{\varepsilon} = (0, 0, \varepsilon_z)$, given in Eq. (C2), we see clearly that the unique term which

will be included into the dipole calculation of the transition $\text{HH}_1 \rightarrow \text{HH}_2$ or in the general case $\text{HH}_1 \rightarrow \text{HH}_n$ is

$$2(\gamma_1 - 2\gamma_2) \left(-i \frac{\partial}{\partial z} \right), \quad (10)$$

where²⁵

$$(\gamma_1 - 2\gamma_2) = 1 + \frac{E_{PX}}{3} \left(\frac{2}{E_G + E_{GC}} + \frac{1}{E_G + E_{GC} + \Delta_C} \right). \quad (11)$$

First from Eqs. (10) and (11), we see that, besides the remote bands, the only conduction band which influences the transition $\text{HH}_1 \rightarrow \text{HH}_n$ parallel to the growth axis is the p -type conduction band via the interband matrix element E_{PX} . This result is in contrast with the result reported in Ref. 11 indicating that both s - and p -type conduction bands play the same role in z -polarized optical transitions when k_{\parallel} increases. We emphasize that the s -type conduction band influence occurs only for $k_{\parallel} \neq 0$. Second, because of the symmetry of the quantum well and the operator $\hat{k}_z = -i \partial / \partial z$ is odd, only transitions from HH_1 to HH_n where n is even are allowed. We note that expression (10) is equivalent to an effective mass approach which gives the well-known selection rule for intersubband transitions and includes implicitly the p -type conduction band effect on the $\text{HH}_1 \rightarrow \text{HH}_n$ transition. From the matrix $\boldsymbol{\varepsilon} \cdot \nabla_{\mathbf{k}} H_k$ in the case $\boldsymbol{\varepsilon} = (\varepsilon_x, \varepsilon_y, 0)$ [Eq. (C1) in Appendix C] we expect no transition $\text{HH}_1 \rightarrow \text{HH}_n$ to be allowed for light polarized parallel to the layer plane when $k_{\parallel} = 0$. Figures 9(a) and 9(b) show the dipole matrix element for the $\text{HH}_1 \rightarrow \text{HH}_2$ transition calculated with the 14- and 6-band models as dashed and solid lines respectively. For light polarized along the growth axis, the transition is allowed at $k_{\parallel} = 0$ while for light polarized parallel to the layer the transition is forbidden. We find numerically a zero value for the dipole element $\text{HH}_1 \rightarrow \text{HH}_3$ at $k_{\parallel} = 0$ in z and x polarization. These results are in agreement with the general selection rule of the transitions $\text{HH}_1 \rightarrow \text{HH}_n$.

We now turn to the case of the $\text{HH}_1 \rightarrow \text{LH}_n$ transitions at $k_{\parallel} = 0$. While the light hole is strongly mixed with the spin-orbit split-off band at $k_{\parallel} = 0$, two matrix elements are involved into the $\text{HH}_1 \rightarrow \text{LH}_n$ transitions. For light polarized parallel to the layer plane, the first and second terms are given by [see Eq. (C1)]

$$(\boldsymbol{\varepsilon}_{\parallel} \cdot \nabla_{\mathbf{k}} H_k)_{\text{HH}_1, \text{LH}_1} = 2\sqrt{3} \gamma_3 \left(-i \frac{\partial}{\partial z} \right) \quad (12)$$

and

$$(\boldsymbol{\varepsilon}_{\parallel} \cdot \nabla_{\mathbf{k}} H_k)_{\text{HH}_1, \text{SO}_1} = \sqrt{6} \gamma_3 \left(-i \frac{\partial}{\partial z} \right), \quad (13)$$

where²⁵

$$\gamma_3 = \frac{E_P}{6E_G} + \frac{E_{PX}}{6(E_G + E_{GC})}. \quad (14)$$

The transition $\text{HH}_1 \rightarrow \text{LH}_n$ for light polarized parallel to the layer plane at $k_{\parallel} = 0$ is governed by the γ_3 parameter and

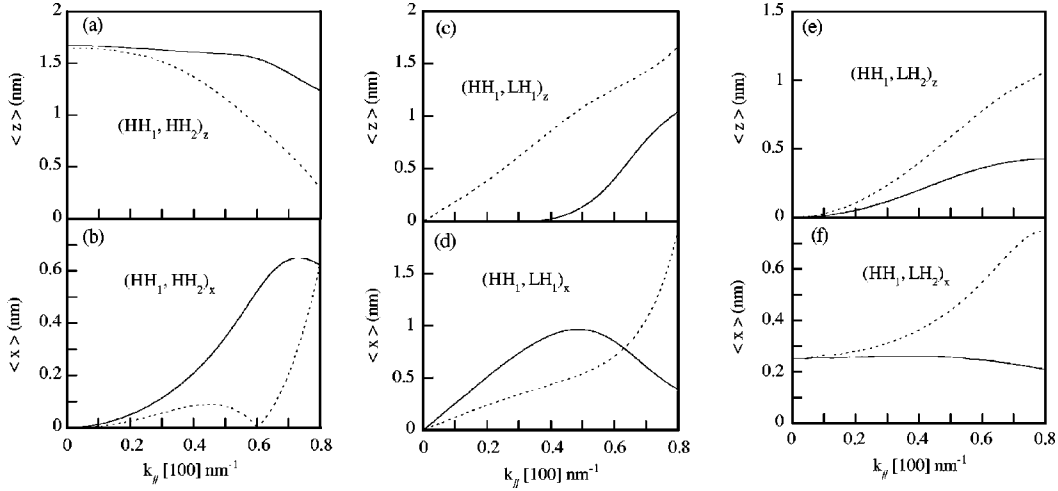


FIG. 9. (a), (b) Dipolar matrix element in nm for the transition $HH_1 \rightarrow HH_2$ (a) along the z axis and (b) along the x axis. The dipole is calculated along the $[100]$ direction. The solid (dashed) lines correspond to the 6- (14-) band formalism. (c), (d) Dipolar matrix element in nm for the transition $HH_1 \rightarrow LH_1$ (c) along the z axis and (d) along the x axis. The dipole is calculated along the $[100]$ direction. In both figures the solid (dashed) lines correspond to the 6- (14-) band formalism. (e), (f) Dipolar matrix element in nm for the transition $HH_1 \rightarrow LH_2$ (e) along the z axis and (f) along x axis. The dipole is calculated along the $[100]$ direction. In both figures the solid (dashed) lines correspond to the 6- (14-) band formalism.

the odd operator $-i \partial / \partial z$. Following the set of equations (12)–(14), we conclude (i) that at $k_{\parallel} = 0$ the transition $HH_1 \rightarrow LH_n$ for light polarized in the layer plane is due to the influence of both s - and p -type conduction bands with an equal weight as E_p / E_G is close to $E_{pX} / (E_G + E_{GC})$ [Eq. (14)] and (ii) this transition is allowed for the LH_n -confined state for even values of n as in LH_2 [Eqs. (12) and (13)].

According to the matrix $\epsilon_z \cdot \nabla_{\mathbf{k}} H_{\mathbf{k}}$ given in Appendix C for the case $\epsilon = (0, 0, \epsilon_z)$ which does not exhibit terms coupling heavy holes with light holes and the spin-orbit split-off band, we also conclude (iii) that no transition $HH_1 \rightarrow LH_n$ for light polarized along the growth axis is allowed at $k_{\parallel} = 0$. The dipole matrix elements for the transitions $HH_1 \rightarrow LH_1$ and $HH_1 \rightarrow LH_2$ are given in Figs. 9(c), (d) and 9(e), (f) along the $[100]$ direction for both 6- and 14-band models. Figures 9(c) and 9(e) correspond to the z polarization while Figs. 9(d) and 9(f) correspond to the in-plane polarization. We observe that the conclusion (ii) is verified for x polarization and that the condition (iii) is verified for z polarization.

When comparing the dipole matrix element values obtained from both models as reported in Fig. 9, we observe that at $k_{\parallel} = 0$ both models are in good agreement but that differences appear very rapidly as k_{\parallel} increases. Since the calculation of the dipole elements provides a theoretical support to the experimental measurements like the absorption in doped structures,³ we point out that the theoretical general trends obtained with one of both models should be taken with a margin of error given by the variation between both models. As an example we show in Fig. 10 the absorption spectrum in both x and z polarizations calculated with the average value of the dipole elements in the $(k_x, k_y, 0)$ plane. The comparison is performed for a p -type doping level of $p = 2.8 \times 10^{18} \text{ cm}^{-3}$ ($p_{2D} = 1.4 \times 10^{12} \text{ cm}^{-2}$ for a 5-nm-thick quantum well) and considering an homogeneous broadening of 10 meV (full width at maximum). We see that the 6-band model gives a much higher absorption amplitude (factor of

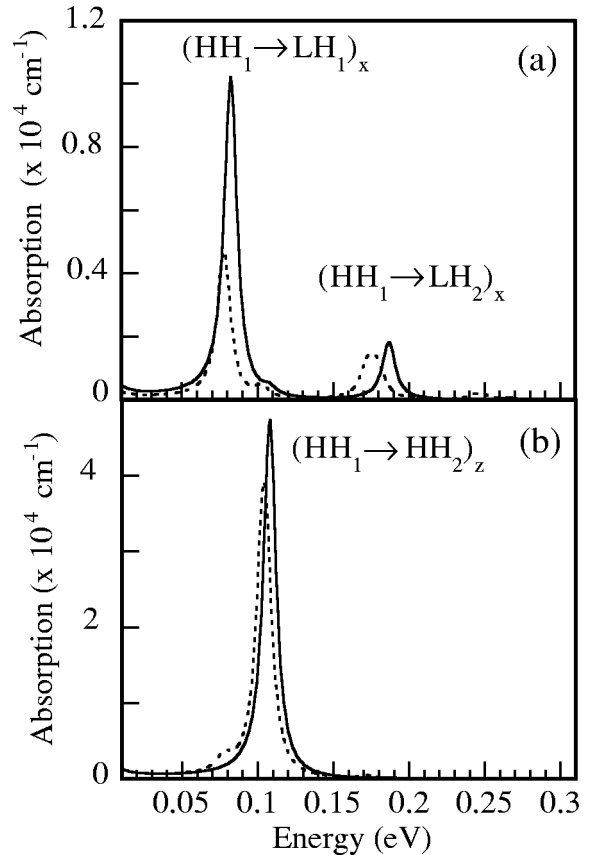


FIG. 10. Calculated absorption spectrum of a 5-nm-thick $\text{Si}_{0.5}\text{Ge}_{0.5}$ quantum well, p doped with a hole concentration of $2.8 \times 10^{18} \text{ cm}^{-3}$. 6-band model (solid line) and 14-band model (dashed line). (a) corresponds to a light polarization along the x axis and (b) corresponds to a light polarized along the z axis.

2) for the $\text{HH}_1 \rightarrow \text{LH}_1$ transition for light polarized parallel to the layer plane and an amplitude enhancement by 20% for the transition $\text{HH}_1 \rightarrow \text{HH}_2$ for light polarized parallel to the growth axis. We also observe a weak shift between the resonance energies obtained with both models. This shift is associated with the difference in the energy band diagrams as reported in Fig. 6. For a doping level of $6.4 \times 10^{11} \text{ cm}^{-2}$ the variation of the absorption amplitude reaches 10% for the transition $\text{HH}_1 \rightarrow \text{HH}_2$ for light polarized parallel to the growth axis and is close to 50% for the $\text{HH}_1 \rightarrow \text{LH}_1$ transition for light polarized parallel to the layer plane. We conclude that the difference between both models should be considered when choosing a formalism to describe the experimental results, in particular if the system exhibits a high density of holes.

IV. AXIAL APPROXIMATION WITH THE 14-BAND MODEL

In the 4×4 Luttinger-Kohn Hamiltonian, the axial (or cylindrical) approximation consists in taking $\gamma_d = 0$, which does not mean $\gamma_2 = \gamma_3$ elsewhere. This approximation leads to an energy which depends on $(k_x^2 + k_y^2)^{1/2}$ (Refs. 21,23, and 24). The axial approximation can be used in the 6×6 Luttinger-Kohn Hamiltonian. In the 8×8 Pidgeon-Brown Hamiltonian, the Pk interaction between the conduction and valence bands is isotropic and the same approximation keeps cylindrical symmetry: it is thus enough to change the Luttinger-like parameters of the 8×8 Hamiltonian. On the contrary, in the 14×14 Hamiltonian, the P_{Xk} interaction is anisotropic and whatever the values of the Luttinger-like parameters the energy depends on the direction and cannot be averaged via the Luttinger-like parameters, as is shown hereafter.

Following an idea of Ref. 21, we first show that we can lower the anisotropy of the 14×14 matrix: to compensate the anisotropy of the P_{Xk} interaction inside the valence band we change the influence of the remote bands which are included by second-order perturbation via the Luttinger-like parameters. A short calculation from Eq. (B2) in Appendix B leads to the following value of γ'_d in the term of Eq. (B1):

$$\gamma'_d = \frac{\gamma'_3 - \gamma'_2}{2} = -\frac{E_{PX}}{6} \frac{1}{E_G + E_{GC}}. \quad (15)$$

We note that when projecting the 14 -band $\mathbf{k}\cdot\mathbf{p}$ matrix onto the $[\Gamma_8^+, \Gamma_7^+]$ (see Appendix B) with γ'_d given by Eq. (15) and by considering second-order perturbation of the conduction band on the valence band, we obtain the 6 -band $\mathbf{k}\cdot\mathbf{p}$ matrix (Appendix A) with $\gamma_d = 0$. In Fig. 11, we show the dispersion curves of the valence band in bulk silicon along the $[100]$, $[210]$, and $[110]$ directions. These dispersion curves are obtained with the 14×14 matrix in which we have replaced γ'_d by Eq. (15). For small wave vectors—i.e., for k_{\parallel} lower than 1 nm^{-1} —the energies are weakly dependent on the k_{\parallel} direction, thus leading to a nearly cylindrical symme-

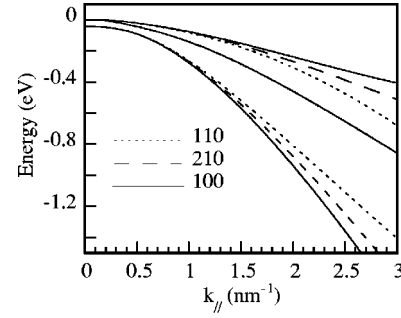


FIG. 11. Valence band dispersion curve of bulk silicon calculated with the 14×14 matrix and taking the γ'_d given by Eq. (15) in the term C' inside the $[\Gamma_8^+, \Gamma_7^+]$. The dispersion curves along $[100]$, $[210]$, and $[110]$ appear as solid, dashed, and dotted lines, respectively. The anisotropy of the valence band evolves continuously between the directions $[100]$ and $[110]$. The anisotropy effect of the p -type conduction band on the valence band cannot be avoided when the electronic wave vector increases when using the 14 -band model. If we use the axial approximation proposed in Ref. 21 with the 6 -band model by putting $\gamma_d = 0$ in the C term of the 6×6 matrix, the dispersion curve is strictly the same for the three directions $[100]$, $[210]$, and $[110]$ and more generally for any direction $[k_x, k_y, 0]$.

try. As the wave vector increases, the energies become very sensitive to the direction and the in-plane isotropy behavior is lost. This is due to the fact that the interband matrix elements P_{Xk} become too large as compared to the second-order perturbation as reported in Eq. (15). This feature leads to an anisotropy of the valence band in the $[k_x, k_y, 0]$ plane when k increases. Therefore when including the p -type conduction band effect exactly in the valence band calculation as is made with the 14 -band model, the axial approximation usually done into the Luttinger-Kohn or Pidgeon-Brown Hamiltonian by a method equivalent to that proposed in Refs. 21 and 24 does not give valence band dispersion with a cylindrical symmetry.

V. CONCLUSION

We have presented a comparison between a 6 -band and a 14 -band $\mathbf{k}\cdot\mathbf{p}$ formalism to describe the valence band structure and intersubband optical matrix elements of SiGe/Si heterostructures. In the bulk, a discrepancy between both models appears for wave vectors larger than 0.5 nm^{-1} . The validity of the 14 -band model at large wave vectors was inferred from a comparison with a more complete calculation using a sp^3s^* formalism. In the case of SiGe/Si quantum wells, the origin of the optical selection rules was discussed on the basis of the projection of the envelope function on the different subbands. The role of the s -type and p -type conduction bands on the selection rules was emphasized. The dipolar matrix elements of the $\text{HH}_1 \rightarrow \text{HH}_2$ and $\text{HH}_1 \rightarrow \text{LH}_2$ intersubband transitions were calculated for the in-plane and z directions. We have found that the 6 -band formalism leads to an overestimation of the amplitude of the intersubband absorption as compared to the 14 -band formalism. We have finally shown that the axial approximation is not valid for the 14 -band formalism.

ACKNOWLEDGMENTS

We thank S. Richard and F. Aniel for providing the set of parameters used to compute the dispersion diagram with the sp^3s^* method.

APPENDIX A: THE 6-BAND HAMILTONIAN

By applying the H_k Hamiltonian to the 6-fold valence band space defined in Table I and written in the order $|+, \frac{3}{2}\rangle$, $|+, \frac{1}{2}\rangle$, $|+, -\frac{1}{2}\rangle$, $|+, -\frac{3}{2}\rangle$, $|+, +\rangle$, $|+, -\rangle$, the 6×6 Hamiltonian is given by

$$H_k^{6 \times 6} = \begin{pmatrix} -\gamma_1 \check{k}^2 + A & B & C & 0 & \frac{B}{\sqrt{2}} & \sqrt{2}C \\ cc & -\gamma_1 \check{k}^2 - A & 0 & C & -\sqrt{2}A & -\sqrt{\frac{3}{2}}B \\ cc & 0 & -\gamma_1 \check{k}^2 - A & -B & -\sqrt{\frac{3}{2}}B^* & \sqrt{2}A \\ 0 & cc & cc & -\gamma_1 \check{k}^2 + A & -\sqrt{2}C^* & \frac{B^*}{\sqrt{2}} \\ cc & cc & cc & cc & -\Delta - \gamma_1 \check{k}^2 & 0 \\ cc & cc & cc & cc & 0 & -\Delta - \gamma_1 \check{k}^2 \end{pmatrix}, \quad (\text{A1})$$

where

$$\begin{aligned} A &= \gamma_2(2\check{k}_z^2 - \check{k}_\rho^2), \\ B &= 2\sqrt{3}\gamma_3\check{k}_z(\check{k}_x - i\check{k}_y), \\ C &= \sqrt{3}[\gamma_m\check{k}_-^2 - \gamma_d\check{k}_+^2], \end{aligned}$$

with $\check{k}_\pm = \check{k}_x \pm i\check{k}_y$ and $\check{k}_\rho^2 = \check{k}_x^2 + \check{k}_y^2$, where $\check{k}_\alpha = \sqrt{\frac{\hbar^2}{2m_0}}k_\alpha$, $\alpha = x, y, z, \rho, +, -$, and $\gamma_m = (\gamma_3 + \gamma_2)/2$, $\gamma_d = (\gamma_3 - \gamma_2)/2$. The numerical values of E_p , E_{px} , E_G , E_{GC} , Δ , Δ_C , and γ_j are given in Table III.

The strain Hamiltonian we used in the quantum well calculation with the six-band model is given in the 6-dimensional spinor basis $\{|+, \frac{3}{2}\rangle, |+, \frac{1}{2}\rangle, |+, -\frac{1}{2}\rangle, |+, -\frac{3}{2}\rangle, |+, +\rangle, |+, -\rangle\}$ by

$$H_S = \begin{pmatrix} a_V\varepsilon - b_V\varepsilon_{\parallel\perp} & 0 & 0 & 0 & 0 & 0 \\ 0 & a_V\varepsilon + b_V\varepsilon_{\parallel\perp} & 0 & 0 & \sqrt{2}b_V\varepsilon_{\parallel\perp} & 0 \\ 0 & 0 & a_V\varepsilon + b_V\varepsilon_{\parallel\perp} & 0 & 0 & -\sqrt{2}b_V\varepsilon_{\parallel\perp} \\ 0 & 0 & 0 & a_V\varepsilon + b_V\varepsilon_{\parallel\perp} & 0 & 0 \\ 0 & \sqrt{2}b_V\varepsilon_{\parallel\perp} & 0 & 0 & a_V\varepsilon & 0 \\ 0 & 0 & -\sqrt{2}b_V\varepsilon_{\parallel\perp} & 0 & 0 & a_V\varepsilon \end{pmatrix}, \quad (\text{A2})$$

where $\varepsilon_{\parallel\perp} = \varepsilon_{\parallel} - \varepsilon_{\perp}$, $\varepsilon_{\perp} = \varepsilon_{zz} = -2(C_{12}/C_{11})\varepsilon_{\parallel}$, and $\varepsilon_{\parallel} = \varepsilon_{xx} = \varepsilon_{yy} = (a_{\text{Si}} - a_{\text{Si}_{1-x}\text{Ge}_x})/(a_{\text{Si}_{1-x}\text{Ge}_x})$ where a_{Si} and $a_{\text{Si}_{1-x}\text{Ge}_x}$ are the lattice constants of the substrate material (Si) and the well material ($\text{Si}_{1-x}\text{Ge}_x$), respectively. The deformation potential parameter and lattice constant are given in Table II.

APPENDIX B: THE 14-BAND HAMILTONIAN

1. 14×14 $\mathbf{k} \cdot \mathbf{p}$ matrix

In the basis spinor at $k=0$ given in Table I and written in the order

$$\begin{aligned} \Gamma_8^- : & |-, \frac{3}{2}\rangle, |-, \frac{1}{2}\rangle, |-, -\frac{1}{2}\rangle, |-, -\frac{3}{2}\rangle, \Gamma_6^- : |-, +\rangle, |-, -\rangle, \Gamma_7^- : |+\rangle, |-\rangle, \\ \Gamma_8^+ : & |+, \frac{3}{2}\rangle, |+, \frac{1}{2}\rangle, |+, -\frac{1}{2}\rangle, |+, -\frac{3}{2}\rangle, \Gamma_7^+ : |+, +\rangle, |+, -\rangle, \end{aligned}$$

the 14×14 Hamiltonian is given by

$$H_k^{14 \times 14}$$

$$= \begin{pmatrix} E_{8-}^H & B_C & C_C & 0 & \frac{1}{\sqrt{2}}B_{\Delta C} & \sqrt{2}C_{\Delta C} & 0 & 0 & 0 & \frac{1}{\sqrt{3}}P_X^+ & \frac{1}{\sqrt{3}}P_X^z & 0 & \frac{1}{\sqrt{6}}P_X^+ & \sqrt{\frac{2}{3}}P_X^z \\ cc & E_{8-}^L & 0 & C_C & -\sqrt{2}A_{\Delta C} & -\sqrt{\frac{3}{2}}B_{\Delta C} & 0 & 0 & \frac{-1}{\sqrt{3}}P_X^- & 0 & 0 & \frac{1}{\sqrt{3}}P_X^z & 0 & \frac{-1}{\sqrt{2}}P_X^+ \\ cc & 0 & E_{8-}^L & -B_C & -\sqrt{\frac{3}{2}}B_{\Delta C}^* & \sqrt{2}A_{\Delta C} & 0 & 0 & \frac{-1}{\sqrt{3}}P_X^z & 0 & 0 & \frac{-1}{\sqrt{3}}P_X^+ & \frac{1}{\sqrt{2}}P_X^- & 0 \\ 0 & cc & cc & E_{8-}^H & -\sqrt{2}C_{\Delta C}^* & \frac{1}{\sqrt{2}}B_{\Delta C}^* & 0 & 0 & 0 & \frac{-1}{\sqrt{3}}P_X^z & \frac{1}{\sqrt{3}}P_X^- & 0 & \sqrt{\frac{2}{3}}P_X^z & \frac{-1}{\sqrt{6}}P_X^- \\ cc & cc & cc & cc & E_{6-} & 0 & 0 & 0 & \frac{-1}{\sqrt{6}}P_X^- & 0 & \frac{-1}{\sqrt{2}}P_X^+ & -\sqrt{\frac{2}{3}}P_X^z & 0 & 0 \\ cc & cc & cc & cc & 0 & E_{6-} & 0 & 0 & -\sqrt{\frac{2}{3}}P_X^z & \frac{1}{\sqrt{2}}P_X^- & 0 & \frac{1}{\sqrt{6}}P_X^+ & 0 & 0 \\ 0 & 0 & 0 & 0 & 0 & 0 & E_{7-} & 0 & \frac{-1}{\sqrt{2}}P^+ & \sqrt{\frac{2}{3}}P^z & \frac{1}{\sqrt{6}}P^- & 0 & \frac{1}{\sqrt{3}}P^z & \frac{1}{\sqrt{3}}P^- \\ 0 & 0 & 0 & 0 & 0 & 0 & 0 & E_{7-} & 0 & \frac{-1}{\sqrt{6}}P^+ & \sqrt{\frac{2}{3}}P^z & \frac{1}{\sqrt{2}}P^- & \frac{1}{\sqrt{3}}P^+ & \frac{-1}{\sqrt{3}}P^z \\ 0 & cc & cc & 0 & cc & cc & cc & 0 & E_{8+}^H & B' & C' & 0 & \frac{1}{\sqrt{2}}B_{\Delta}' & \sqrt{2}C_{\Delta}' \\ cc & 0 & 0 & cc & 0 & cc & cc & cc & cc & E_{8+}^L & 0 & C' & -\sqrt{2}A & -\sqrt{\frac{3}{2}}B \\ cc & 0 & 0 & cc & cc & 0 & cc & cc & cc & 0 & E_{8+}^L & -B' & -\sqrt{\frac{3}{2}}B_{\Delta}'^* & \sqrt{2}A_{\Delta}' \\ 0 & cc & cc & 0 & cc & cc & 0 & cc & 0 & cc & cc & E_{8+}^H & -\sqrt{2}C_{\Delta}'^* & \frac{1}{\sqrt{2}}B_{\Delta}'^* \\ cc & 0 & cc & cc & 0 & 0 & cc & cc & cc & cc & cc & cc & E_{7+} & 0 \\ cc & cc & 0 & cc & 0 & 0 & cc & cc & cc & cc & cc & cc & 0 & E_{7+} \end{pmatrix}.$$

(B1)

In the following, the index j refers to the three indexes (1,2,3).

2. Off-diagonal matrix elements inside the $[\Gamma_8^+, \Gamma_7^+]$ valence band subspace

The off-diagonal matrix elements inside the valence band subspace are given by:

$$\begin{aligned} A' &= \gamma_2'(2\check{k}_z^2 - \check{k}_\rho^2), & A_{\Delta}' &= \gamma_{\Delta 2}'(2\check{k}_z^2 - \check{k}_\rho^2), \\ B' &= 2\sqrt{3}\gamma_3'\check{k}_z\check{k}_-, & B_{\Delta}' &= 2\sqrt{3}\gamma_{\Delta 3}'\check{k}_z\check{k}_-, \\ C' &= \sqrt{3}(\gamma_m'\check{k}_-^2 - \gamma_d'\check{k}_+^2), & C_{\Delta}' &= \sqrt{3}(\gamma_{\Delta m}'\check{k}_-^2 - \gamma_{\Delta d}'\check{k}_+^2), \end{aligned}$$

with

$$\begin{aligned} \gamma_m' &= (\gamma_3' + \gamma_2')/2, & \gamma_d' &= (\gamma_3' - \gamma_2')/2, & \gamma_{\Delta m}' &= (\gamma_{\Delta 3}' + \gamma_{\Delta 2}')/2, \\ \gamma_{\Delta d}' &= (\gamma_{\Delta 3}' - \gamma_{\Delta 2}')/2. \end{aligned}$$

In the 14-band model, the effect of the remote bands on the valence band is taken into account by the parameter γ_j' ($j = 1, 2, 3$). While the Luttinger parameters γ_j contain the ef-

fect of all the bands including $[\Gamma_8^-, \Gamma_6^-, \Gamma_7^-]$, the γ_j' are related to the Luttinger parameters γ_j available in Table III by the following relations:²⁵

$$\gamma_1' = \gamma_1 - \frac{E_P}{3E_G} - \frac{E_{PX}}{3} \left(\frac{1}{E_G + E_{GC}} + \frac{1}{E_G + E_{GC} + \Delta_C} \right),$$

$$\gamma_2' = \gamma_2 - \frac{E_P}{6E_G} + \frac{E_{PX}}{6(E_G + E_{GC})},$$

$$\gamma_3' = \gamma_3 - \frac{E_P}{6E_G} - \frac{E_{PX}}{6(E_G + E_{GC})}. \quad (\text{B2})$$

Since the spin-orbit energy Δ is small as compared to the energy difference between the valence band and the far level outside the $[\Gamma_8^-, \Gamma_6^-, \Gamma_7^-, \Gamma_8^+, \Gamma_7^+]$, we use $\gamma_j' = \gamma_{\Delta j}'$ (Ref. 25).

3. Off-diagonal matrix elements inside the $[\Gamma_8^-, \Gamma_6^-]$ conduction bands

We define the off-diagonal matrix elements inside the $[\Gamma_8^-, \Gamma_6^-]$ conduction bands as:

$$\begin{aligned} A_C &= \tilde{\gamma}_{C2}(2\tilde{k}_z^2 - \tilde{k}_\rho^2), & A_{\Delta C} &= \tilde{\gamma}_{\Delta C2}(2\tilde{k}_z^2 - \tilde{k}_\rho^2), \\ B_C &= 2\sqrt{3}\tilde{\gamma}_{C3}\tilde{k}_z\tilde{k}_-, & B_{\Delta C} &= 2\sqrt{3}\tilde{\gamma}_{\Delta C3}\tilde{k}_z\tilde{k}_-, \\ C_C &= \sqrt{3}[\tilde{\gamma}_{C2}(\tilde{k}_x^2 - \tilde{k}_y^2) - 2i\tilde{\gamma}_{C3}\tilde{k}_x\tilde{k}_y], \\ C_{\Delta C} &= \sqrt{3}[\tilde{\gamma}_{\Delta C2}(\tilde{k}_x^2 - \tilde{k}_y^2) - 2i\tilde{\gamma}_{\Delta C3}\tilde{k}_x\tilde{k}_y]. \end{aligned}$$

The general expression of the Luttinger-like parameter $\tilde{\gamma}_{Cj}$ into the off-diagonal term inside the p -type conduction band subspace is given by the following set of equations:²⁵

$$\tilde{\gamma}_{Cj} = \tilde{\gamma}_{\Delta Cj};$$

$$\begin{aligned} \tilde{\gamma}_{C1} &= \gamma_{C1} + \frac{E_{PX}}{3} \left(\frac{1}{E_G + E_{GC} + \Delta_C} + \frac{1}{E_G + E_{GC} + \Delta_C + \Delta} \right), \\ \tilde{\gamma}_{C2} &= \gamma_{C2} - \frac{E_{PX}}{6(E_G + E_{GC} + \Delta_C + \Delta)}, \\ \tilde{\gamma}_{C3} &= \gamma_{C3} + \frac{E_{PX}}{6(E_G + E_{GC} + \Delta_C + \Delta)}. \end{aligned} \quad (\text{B3})$$

The γ_{Cj} are the Luttinger parameters for the p -type conduction band which includes the whole band effect on the $[\Gamma_8^-, \Gamma_6^-]$ subspace. The parameters $\tilde{\gamma}_{Cj}$ account for the remote band effect on the $[\Gamma_8^-, \Gamma_6^-]$ p -type conduction bands without the valence band $[\Gamma_8^+, \Gamma_7^+]$ and the conduction band Γ_7^- . In the Hamiltonian which includes off-diagonal terms in the subspace $[\Gamma_8^-, \Gamma_6^-]$, the $\tilde{\gamma}_{Cj}$ parameters are related to the γ_{Cj} parameters by the set of equations (B3). We can note that in semiconductors with inversion symmetry such as Si and Ge, the coupling between the Γ_7^- and $[\Gamma_8^-, \Gamma_6^-]$ vanishes. As opposed to the case of GaAs,²⁶ the set of equations (B3) would contain the dipolar matrix elements between Γ_7^- and $[\Gamma_8^-, \Gamma_6^-]$. When taking $\gamma_{Cj}=0$ in Eqs. (B3), we consider that the result of the whole band effect on the p -type conduction band $[\Gamma_8^-, \Gamma_6^-]$ is to lead to a flat band. When the remote bands are not taken into account inside the $[\Gamma_8^-, \Gamma_6^-]$ band, we take $\tilde{\gamma}_{Cj}=0$ in all nondiagonal terms and we take $\tilde{\gamma}_{C1}=-1$ and $\tilde{\gamma}_{C2}=0$ in the diagonal terms. In this way we take the nonperturbed terms of the Hamiltonian H_k inside $[\Gamma_8^-, \Gamma_6^-]$. While the s -type conduction band behavior is close to the free electron energy dispersion near the Γ point, we do not include the remote band effect on the Γ_7^- band.

4. Interband matrix elements

The momentum matrix elements are defined as

$$\begin{aligned} P^\pm &= Pk_\pm, \\ P^z &= Pk_z, \end{aligned}$$

$$P_X^\pm = P_X k_\pm,$$

$$P_X^z = P_X k_z.$$

Here P and P_X are the interband matrix elements defined as

$$P = \frac{\hbar}{m_0} \langle S | p_x | iX \rangle,$$

$$P_X = \frac{\hbar}{m_0} \langle Z_C | p_x | iY \rangle = \frac{\hbar}{m_0} \langle Y_C | p_x | iX \rangle = \frac{\hbar}{m_0} \langle X_C | p_x | iZ \rangle.$$

The parameters E_P and E_{PX} are defined as $E_{PX} = (2m_0/\hbar^2)P_X^2$ and $E_P = (2m_0/\hbar^2)P^2$.

We note that the inclusion of remote bands by second-order perturbation leads to the appearance of interband off-diagonal terms in second order of k in the following expressions:

$$\sum_i \langle S | \mathbf{k} \cdot \mathbf{p} | i \rangle \langle i | \mathbf{k} \cdot \mathbf{p} | X \rangle \frac{1}{2} \left(\frac{1}{E_S - E_i} + \frac{1}{E_X - E_i} \right)$$

and

$$\sum_i \langle X_C | \mathbf{k} \cdot \mathbf{p} | i \rangle \langle i | \mathbf{k} \cdot \mathbf{p} | X \rangle \frac{1}{2} \left(\frac{1}{E_{XC} - E_i} + \frac{1}{E_X - E_i} \right),$$

where i is an intermediate far level at energy E_i . Because each involved function is an eigenstate of the inversion symmetry operator of the O_h group and knowing that the valence states have opposite parities with the first p -type and s -type conduction states, these interband terms are equal to zero in our case. When considering T_d crystals like GaAs, these terms are not equal to zero but are usually omitted without any explanation in the literature. As the remote bands are in the most general case far in energy from the first conduction band and valence band, one can suppose that it is very weak as compared to the interband coupling term Pk . A more detailed study concerning semiconductors without inversion symmetry would be necessary to clarify this point.

5. Diagonal matrix elements

The diagonal matrix elements are defined by:

$$E_{8-}^H = E_{8-}^0 - \tilde{\gamma}_{C1}\tilde{k}^2 + A_C,$$

$$E_{8-}^L = E_{8-}^0 - \tilde{\gamma}_{C1}\tilde{k}^2 - A_C,$$

$$E_{6-} = E_{6-}^0 - \tilde{\gamma}_{\Delta C1}\tilde{k}^2,$$

$$E_{7-} = E_{7-}^0 - \tilde{k}^2,$$

$$E_{8+}^H = E_{8+}^0 - \gamma'_1\tilde{k}^2 + A',$$

$$E_{8+}^L = E_{8+}^0 - \gamma'_1\tilde{k}^2 - A',$$

$$E_{7+} = E_{7+}^0 - \gamma'_{\Delta 1}\tilde{k}^2,$$

where

$$E_{8-}^0 = E_G + E_{GC} + \Delta_C,$$

$$E_{6-}^0 = E_G + E_{GC},$$

$$E_{7-}^0 = E_G,$$

$$E_{8+}^0 = 0,$$

$$E_{7+}^0 = -\Delta,$$

and

$$\check{k}^2 = \frac{\hbar^2}{2m_0} k^2.$$

The spin-orbit energies are defined as

$$\Delta = \frac{3\hbar}{4m_0^2 c^2} \langle iX | [\nabla U \wedge \mathbf{p}]_y | Z \rangle,$$

$$\Delta_C = \frac{3\hbar}{4m_0^2 c^2} \langle iX_C | [\nabla U \wedge \mathbf{p}]_y | Z_C \rangle.$$

The numerical values of E_P , E_{PX} , E_G , E_{GC} , Δ , Δ_C , and γ_j are given in Table III.

6. Strain Hamiltonian

In the quantum well calculation, the subband dispersion was obtained from the $H_k^{14 \times 14}$ Hamiltonian onto which we expand the 8×8 strain Hamiltonian H_S and the potential V . In the 8-dimensional spinor basis $\{|+\rangle, |-\rangle, |+\frac{3}{2}\rangle, |+\frac{1}{2}\rangle, |+\frac{1}{2}\rangle, |+\frac{3}{2}\rangle, |+\frac{3}{2}\rangle, |+\frac{1}{2}\rangle\}$ (see Table I) the 8×8 H_S is given by

$$H_S = \begin{pmatrix} a_C \varepsilon & 0 & 0 & 0 & 0 & 0 & 0 & 0 \\ 0 & a_C \varepsilon & 0 & 0 & 0 & 0 & 0 & 0 \\ 0 & 0 & a_V \varepsilon - b_V \varepsilon_{\parallel\perp} & 0 & 0 & 0 & 0 & 0 \\ 0 & 0 & 0 & a_V \varepsilon + b_V \varepsilon_{\parallel\perp} & 0 & 0 & \sqrt{2} b_V \varepsilon_{\parallel\perp} & 0 \\ 0 & 0 & 0 & 0 & a_V \varepsilon + b_V \varepsilon_{\parallel\perp} & 0 & 0 & -\sqrt{2} b_V \varepsilon_{\parallel\perp} \\ 0 & 0 & 0 & 0 & 0 & a_V \varepsilon - b_V \varepsilon_{\parallel\perp} & 0 & 0 \\ 0 & 0 & 0 & \sqrt{2} b_V \varepsilon_{\parallel\perp} & 0 & 0 & a_V \varepsilon & 0 \\ 0 & 0 & 0 & 0 & -\sqrt{2} b_V \varepsilon_{\parallel\perp} & 0 & 0 & a_V \varepsilon \end{pmatrix}, \quad (\text{B4})$$

where $\varepsilon_{\parallel\perp} = \varepsilon_{\parallel} - \varepsilon_{\perp}$, $\varepsilon_{\perp} = \varepsilon_{zz} = -2(C_{12}/C_{11})\varepsilon_{\parallel}$, and $\varepsilon_{\parallel} = \varepsilon_{xx} = \varepsilon_{yy} = (a_{\text{Si}} - a_{\text{Si}_{1-x}\text{Ge}_x}) / (a_{\text{Si}_{1-x}\text{Ge}_x})$ where a_{Si} and $a_{\text{Si}_{1-x}\text{Ge}_x}$ are the lattice constants of the substrate material (Si) and the well material ($\text{Si}_{1-x}\text{Ge}_x$), respectively. The deformation potential parameters a_G , b_V and the lattice constants are given in Table II. Since the deformation potential parameters, which are involved inside the p -type conduction band, are not known, we take them arbitrarily equal to zero.

APPENDIX C: THE DIPOLAR MATRIX ELEMENTS

To simplify the discussion in the text we use the standard notation $\text{HH}(\uparrow\downarrow)$, $\text{LH}(\uparrow\downarrow)$, and $\text{SO}(\uparrow\downarrow)$ to design the spin-degenerated heavy-hole $|+\frac{3}{2}\rangle$, light-hole $|+\frac{1}{2}\rangle$, and spin-orbit $|+\frac{3}{2}\rangle$ states, respectively, defined in Table I. The matrix $\varepsilon \cdot \nabla_{\mathbf{k}} H_k$ is derived from the 6×6 H_k matrix in Eq. (A1) at $k_x = k_y = 0$. For light polarized parallel to the layer plane, $\varepsilon = (\varepsilon_x, \varepsilon_y, 0)$ and $k_{\parallel} = 0$:

$$\varepsilon_{\parallel} \cdot \nabla_{\mathbf{k}} H_k = \frac{\hbar^2}{2m_0} \times \begin{pmatrix} \text{HH}\uparrow & \text{LH}\uparrow & \text{LH}\downarrow & \text{HH}\downarrow & \text{SO}\uparrow & \text{SO}\downarrow \\ 0 & 2\sqrt{3}\gamma_3 \varepsilon_- \hat{k}_z & 0 & 0 & \sqrt{6}\gamma_3 \varepsilon_- \hat{k}_z & 0 \\ cc & 0 & 0 & 0 & 0 & -3\sqrt{2}\gamma_3 \varepsilon_- \hat{k}_z \\ 0 & 0 & 0 & -2\sqrt{3}\gamma_3 \varepsilon_- \hat{k}_z & -3\sqrt{2}\gamma_3 \varepsilon_+ \hat{k}_z & 0 \\ 0 & 0 & cc & 0 & 0 & \sqrt{6}\gamma_3 \varepsilon_+ \hat{k}_z \\ cc & 0 & cc & 0 & 0 & 0 \\ 0 & cc & 0 & cc & 0 & 0 \end{pmatrix}, \quad (\text{C1})$$

where $\varepsilon_- = (\varepsilon_x - i\varepsilon_y)$ and $\varepsilon_+ = (\varepsilon_x + i\varepsilon_y)$.

For light polarized along the growth axis, $\varepsilon = (0, 0, \varepsilon_z)$:

$$\varepsilon_z \cdot \nabla_{\mathbf{k}} H_{\mathbf{k}} = \frac{\hbar^2}{2m_0} \times \begin{pmatrix} & \text{HH}\uparrow & \text{LH}\uparrow & \text{LH}\downarrow & \text{HH}\downarrow & \text{SO}\uparrow & \text{SO}\downarrow \\ -2(\gamma_1 - 2\gamma_2)\hat{k}_z & & 0 & 0 & 0 & 0 & 0 \\ 0 & -2(\gamma_1 + 2\gamma_2)\hat{k}_z & & 0 & 0 & -4\sqrt{2}\gamma_2\hat{k}_z & 0 \\ 0 & 0 & -2(\gamma_1 + 2\gamma_2)\hat{k}_z & & 0 & 0 & 4\sqrt{2}\gamma_2\hat{k}_z \\ 0 & 0 & 0 & -2(\gamma_1 - 2\gamma_2)\hat{k}_z & & 0 & 0 \\ 0 & cc & 0 & 0 & 0 & -2\gamma_1\hat{k}_z & 0 \\ 0 & 0 & cc & 0 & 0 & 0 & -2\gamma_1\hat{k}_z \end{pmatrix}. \quad (\text{C2})$$

In both matrices the terms like $\gamma\hat{k}_z$ have explicitly the form $\frac{1}{2}(\gamma\hat{k}_z + \hat{k}_z\gamma)$ with $\hat{k}_z = -i\partial/\partial z$.

*Electronic address: philippe.boucaud@ief.u-psud.fr

¹B.F. Levine, J. Appl. Phys. **74**, R1 (1993).

²J. Faist, F. Capasso, D. Sivco, C. Sirtori, A.L. Hutchinson, S.N.G. Chu, and A.Y. Cho, Science **264**, 553 (1994).

³T. Fromherz, E. Koppensteiner, M. Helm, G. Bauer, J.F. Nützel, and G. Abstreiter, Phys. Rev. B **50**, 15 073 (1994).

⁴N. Rappaport, E. Finkman, T. Bruhnes, P. Boucaud, S. Sauvage, N. Yam, V. Le Thanh, and D. Bouchier, Appl. Phys. Lett. **77**, 3224 (2000).

⁵G. Dehlinger, L. Diehl, U. Gennser, H. Sigg, J. Faist, K. Ensslin, D. Grützmacher, and E. Müller, Science **290**, 2277 (2000).

⁶J.M. Luttinger and W. Kohn, Phys. Rev. **97**, 869 (1955).

⁷J.M. Luttinger, Phys. Rev. **102**, 1030 (1956).

⁸E.O. Kane, J. Phys. Chem. Solids **1**, 249 (1957).

⁹Yia-Chung Chang and R.B. James, Phys. Rev. B **39**, 12 672 (1989).

¹⁰R. People, J.C. Bean, S.K. Sputz, C.G. Bethea, and L.J. Petricolas, Thin Solid Films **222**, 120 (1992).

¹¹S. Ridene, K. Boujdaria, H. Bouchriha, and G. Fishman, Phys. Rev. B **64**, 085329 (2001).

¹²C.R. Pidgeon and R.N. Brown, Phys. Rev. **146**, 575 (1966).

¹³J.R. Chelikowski and M.L. Cohen, Phys. Rev. B **14**, 556 (1976).

¹⁴N. Cavassilas, F. Aniel, K. Boujdaria, and G. Fishman, Phys. Rev.

B **64**, 115207 (2001).

¹⁵P. Boucaud, S. Sauvage, M. Elkurdi, E. Mercier, T. Bruhnes, V. le Thanh, D. Bouchier, O. Kermarrec, Y. Campidelli, and D. Bensahel, Phys. Rev. B **64**, 155310 (2001).

¹⁶G.E. Pikus and G.L. Bir, Sov. Phys. Solid State **1**, 1502 (1960).

¹⁷M.M. Rieger and P. Vogl, Phys. Rev. B **48**, 14 276 (1993).

¹⁸D.J. BenDaniel and C.B. Duke, Phys. Rev. **152**, 683 (1966).

¹⁹G.A. Baraff and D. Gershoni, Phys. Rev. B **43**, 4011 (1991).

²⁰G. Fishman, Phys. Rev. B **52**, 11 132 (1995).

²¹D.A. Broido and L.J. Sham, Phys. Rev. B **31**, 888 (1985).

²²P. Enders, A. Bärwolff, and M. Woerner, Phys. Rev. B **51**, 16 695 (1995).

²³A. Twardowski and C. Hermann, Phys. Rev. B **35**, 8144 (1987).

²⁴M. Altarelli, U. Ekenberg, and A. Fasolino, Phys. Rev. B **32**, 5138 (1985).

²⁵K. Boujdaria, S. Ridene, and G. Fishman, Phys. Rev. B **63**, 235302 (2001).

²⁶P. Pfeffer and W. Zawadzki, Phys. Rev. B **41**, 1561 (1990).

²⁷*Semiconductor, Physics Group IV Elements and III-V Compounds*, edited by O. Madelung, M. Shultz, and H. Weiss, Landolt-Börnstein, New Series Group III, Vol. 17, Pt. a (Springer-Verlag, New York, 1982).